Ni/ZrO_2 catalysts in ethanol steam reforming: inhibition of coke formation by CaO-doping

Valentina Nichele[1], Michela Signoretto[1,], Francesco Pinna[1], Federica Menegazzo[1], Ilenia Rossetti[2], Giuseppe Cruciani[3], Giuseppina Cerrato[4], Alessandro Di Michele[5]*

[1] Molecular Sciences and Nanosystems Dept., Ca' Foscari University, INSTM Unit, Calle Larga Santa Marta 2137, 30123 Venice (Italy).

[2] Chemistry Dept., ISTM-CNR, INSTM Unit, Università degli Studi di Milano, via C. Golgi, 19, 20133 Milan (Italy).

[3] Earth Sciences Dept., University of Ferrara, via Saragat 1, 44100 Ferrara (Italy).

[4] Chemistry Dept. & NIS Centre of Excellence, University of Turin, INSTM Unit, via P. Giuria 7, 10125 Turin (Italy).

[5] Physics Dept., Università degli Studi di Perugia, Via Pascoli, 06123 Perugia (Italy).

**Corresponding author. E-mail: miky@unive.it*

Phone: +39-041-2348650

Fax: +39-041-2348517

Abstract

In this work the performance of CaO-doped Ni/ZrO_2 catalysts in ethanol steam reforming was studied. The addition of CaO did not affect the morphology or the crystalline structure of the support. On the contrary, Ni reducibility markedly increased. Moreover, the Lewis acidity of zirconia gradually decreased as the CaO content increased, thus inhibiting coke deposition and improving the carbon balance. The addition of a basic oxide helps to prevent some of the side reactions responsible for coke formation and deposition, that can gradually deactivate the catalyst.

Keywords:

Nickel; Zirconia; Ethanol Steam Reforming; CaO-doping; Coking inhibition.

1. Introduction

One of the main challenges for scientists today is to reduce the dependence from fossil fuels. Hydrogen can be the solution to meet the ever growing world energy demand in a clean and sustainable way. It is the ideal candidate for both energy and transport sectors because its combustion does not emit environmental pollutants in the atmosphere. Unfortunately hydrogen is still produced from fossil fuels, so increasing the concerns about global warming. Clean hydrogen can be produced from renewable sources and ethanol emerged as a good candidate for hydrogen production because it has high hydrogen content, it is renewable, easy to store, handle and transport because of its low volatility and non toxicity.
Ethanol steam reforming (ESR) is promising to produce hydrogen in a sustainable way [1-3]. It is an endothermic process which takes place according to the following stoichiometric reaction, Eq.1:

Eq. 1 $$CH_3CH_2OH + 3H_2O \rightleftharpoons 6H_2 + 2CO_2 \qquad (\Delta H^0_{298} = +347.4 \text{ kJ mol}^{-1})$$

including the water-gas shift of the intermediate CO (Eq. 2), which further increases the hydrogen yield:

Eq. 2 $$CO + H_2O \rightleftharpoons CO_2 + H_2 \qquad \Delta H^0_{298} = -41 \text{ kJ/mol}$$

Nevertheless the overall process is a complex network of reactions, such as ethanol dehydrogenation, dehydration or decomposition, which can lead to the formation of several byproducts (acetaldehyde, ethylene and methane respectively) [4, 5]. The formation of coke should also be considered, through the Boudouard reaction ($2CO \rightleftharpoons CO_2 + C$), the decomposition of methane ($CH_4 \rightleftharpoons C + 2H_2$) or the polymerisation of ethylene [6]. Coke deposition can be controlled by properly tuning the operating conditions (*i. e.* steam-to-ethanol ratio, reaction temperature) [7], but the formulation of the catalyst plays a key role as well [6]. Coking is particularly significant around 500°C, where coke forms but is not effectively gasified by steam. Nevertheless, it would be very advantageous being able to operate around this temperature, because some catalyst formulations demonstrated sufficient activity and selectivity, and this relatively low temperature would limit the energy input to the process with respect to common reaction conditions (T > 650°C). Therefore, improving catalyst resistance to coking represents a milestone for the development of low temperature ESR.
Nickel is a highly active and selective active phase for ESR, comparable to noble metals, because of its high capability to break C-C bonds and also to promote the water-gas shift reactions, thus increasing hydrogen yield [8, 9]. It is cheaper and more available than noble metals, although it may

be quickly deactivated by coking and sintering [10]. In particular, coking is thought to occur more promptly over large Ni particles and aggregates [11-14] than over very dispersed crystallites.
With regard to the metal catalyst support, it should possess a good chemical and mechanical resistance and a high surface area, in order to favour the dispersion of the active phase [15, 16]. Our recent results highlighted, on one hand, the importance of the stability of the support in the reaction conditions, on the other the key role of the metal-support interaction in determining both activity and stability of the catalyst [17-19]. In particular, a strong interaction stabilizes the active phase, preserving it from sintering and, thus, from coking phenomena.
Another important property that should be controlled is the acidity of the support. In fact it is well known that the side reactions leading to the formation of coke occur mainly on the acid sites of the support [20-22]. This means that the support plays a key role in determining the reaction pathway and, as a consequence, the selectivity of the process [23, 24].
Ni/ZrO_2 proved to be highly active in steam reforming reactions [17-19]. Its performance was ascribed to some of its features, such as: i) high surface area; ii) high stability under the reaction conditions; iii) strong interactions with the active phase; vi) ability to first adsorb and then dissociate water, thus enhancing the adsorption of steam on its surface and activating the gasification of hydrocarbons [23] and the water-gas shift [25]. Nevertheless, in some conditions, a slight deactivation due to coke deposition was detected [17], probably related to the presence of acid sites on the surface of the support. Zirconia is known to be a solid acid: both acidic OH groups and Lewis acid sites (coordinatively unsaturated, *cus*, Zr^{4+} ions) can be detected on the surface, depending on the synthesis conditions [26-28].
The addition of oxides of alkaline earth metals (*i. e.* CaO, MgO, BaO), which are strong Lewis bases, can decrease the acidity of the support [29-31], thus inhibiting the side reactions responsible for coke deposition. It should be considered that doping can modify also other properties, of both the support (oxygen transport, redox properties) [32, 33] and the catalyst (dispersion of the active phase, interactions between metal and support) [34, 35].
The aim of this work was to properly modify the zirconia support in order to improve the catalytic performance of the catalyst in the steam reforming of ethanol, in particular with regard to resistance to coking. Ni/ZrO_2 catalysts doped with various amounts of CaO were synthesized and characterized. The effect of CaO-doping on both the physico-chemical properties of the materials and the catalytic performance of the samples was evaluated.

2. Experimental Section

2.1 Catalysts preparation

$Zr(OH)_4$ was prepared by a precipitation method [36] at a constant pH of 10. $ZrOCl_2*8H_2O$ (*Sigma-Aldrich, purity ≥ 99.5%*) was dissolved in distilled water and added with a peristaltic pump under vigorous stirring to an ammonia (33%, *Riedel-de Haën*) solution. During the precipitation, the pH value was kept constant at 10.0 ± 0.1 by the continuous addition of a 33% ammonia solution. After the complete addition of the salt solution, the hydroxide suspension was aged for 20 h at 90 °C, then filtered and washed with warm distilled water until it was free from chloride ions ($AgNO_3$ test). The samples were dried overnight at 110 °C.
$Zr(OH)_4$ was impregnated with an aqueous solution containing both the metal ($Ni(NO_3)_2*6H_2O$, *Sigma-Aldrich, purity ≥ 98.5%*) and the dopant ($Ca(NO_3)_2*4H_2O$, *Fluka, purity ≥ 99%*) precursors. The active phase (Ni) and the dopant (CaO) were added to $Zr(OH)_4$ simultaneously by means of the incipient wetness impregnation technique. Ni was kept constant in all the samples (10 wt%), whereas CaO varied (0, 3, 6, 9 wt%). The samples were dried overnight at 110 °C and finally heated (2 °C/min) up to 500 °C in flowing air (30 mL/min STP) and kept at this temperature for 4 hours. The reference sample, Ni/ZrO_2, is labelled as *ZNi*, whereas doped samples are labelled as ZCa_xNi, where Ca_x denotes the CaO amount.

2.2 Catalysts characterization

Specific surface area and pores size distribution were evaluated through N_2 adsorption-desorption isotherms at -196 °C (MICROMERITICS, ASAP 2000 Analyser). Surface area was calculated on the basis of the BET equation [37], whereas the pores size distribution was determined by the BJH method, applied to the N_2 desorption branch of the isotherm [38]. Prior to the analyses the samples were reduced in H_2 flow for 1 h at 500 °C, dried overnight at 110 °C and then outgassed in vacuum at 300 °C for 2 hours.
X-ray powder diffraction (XRD) patterns were measured by a Bruker D8 Advance diffractometer equipped with a Si(Li) solid state detector (SOL-X) and a sealed tube providing Cu Kα radiation. The Rietveld refinement method as implemented in the Bruker TOPAS program was used to obtain the refined unit cell parameters, crystal size, and the quantitative phase analysis for the ZrO_2 support and metal phases in the samples. The crystal size determination is achieved by the integral breadth based calculation of volume weighted mean crystallize sizes assuming intermediate crystallite size broadening modelled by a Voigt function. The samples were reduced in H_2 flow for 1 h at 500 °C before the analysis.
Temperature programmed reduction (TPR) measurements were carried out by placing the catalyst in a quartz reactor and heating in a 5% H_2/Ar mixed gas stream flowing at 40 mL/min at a heating rate of 10 °C/min from 25 to 700 °C. H_2 consumption was monitored by a TCD detector.
Temperature programmed oxidation (TPO) of the spent catalysts was carried out by feeding 40 mL/min of a 10 vol% O_2/He gas mixture while heating by 10°C/min from 25 to 650°C.
O_2 pulse chemisorption measurements were performed at 25 °C by means of a lab-made equipment. Before chemisorption the sample (100 mg) was reduced in H_2 flow (40 mL/min) at 500 °C for 1 hour and then evacuated under helium gas at 500°C for 2 hours to remove all physisorbed hydrogen. A Ni/O_2 chemisorption stoichiometry = 2 was used [39].
In situ FTIR spectra were obtained on a Perkin Elmer 2000 spectrophotometer (4 cm^{-1} resolution, MCT detector). Reduced samples were inspected in the form of self-supporting tablets (~25 mg cm^{-2}). Quartz cells (equipped with KBr windows) connected to a gas vacuum line equipped with rotary and turbomolecular pumps (residual pressure $p < 10^{-5}$ Torr) were used. The samples were activated in oxygen at 300 °C. FTIR spectra of probe molecules (CO) adsorbed thereon were also run, in order to obtain information on surface acidity.
(High-Resolution) Transmission electron microscopy (HR-TEM) images were obtained by using a JEOL JEM 3010UHR (300 kV) TEM fitted with a single crystal LaB_6 filament and an Oxford INCA Energy TEM 200 energy dispersive X-ray (EDX) detector. All samples were dry deposited, after their reduction, on Cu "holey" carbon grids (200 mesh).
SEM images have been obtained using a Field Emission Gun Electron Scanning Microscopy LEO 1525, after metallization with Cr. Elemental composition was determined using Bruker Quantax EDS.
HR-TEM images of spent samples have been obtained using a Philips 208 Transmission Electron Microscope. The samples were prepared by putting one drop of an ethanol dispersion of the catalysts on a copper grid pre-coated with a Formvar film and dried in air.
Micro-Raman sampling was made by an OLYMPUS microscope (model BX40) connected to an ISA Jobin–Yvon model TRIAX320 single monochromator, with a resolution of 1 cm^{-1}. The source of excitation was a Melles Griot 25LHP925 He-Ne laser that was used in single line excitation mode at l=632.8 nm. The power focused on the samples was always less than 2 mW. The scattered Raman photons were detected by a liquid-nitrogen cooled charge coupled device (CCD, Jobin Yvon mod. Spectrum One).

2.3 Catalytic tests: ethanol steam reforming

Activity tests were performed by means of a continuous micropilot plant including an Incoloy 800 downflow reactor (*i.d.* 0.9 cm, length 40 cm) heated by an electric oven connected to an Eurotherm 3204 TIC. The catalysts were pressed, ground and sieved into 0.15-0.25 mm particles and *ca*. 0.5 g were loaded into the reactor after dilution 1:3 (vol/vol) with SiC of the same particle size. The void part of the reactor over and below the catalyst bed has been filled with quarts beads (0.5-1 mm size). The catalysts were activated in 50 cm^3/min of a 20 vol% H_2/N_2 gas mixture, while heating by 10 °C/min up to 500 °C, then kept for 1 h. During activity testing 0.017 cm^3/min of a 3:1 (mol/mol) H_2O:CH_3CH_2OH liquid mixture were fed to the reactor by means of a Hitachi, mod. L7100, HPLC pump. 56 cm^3/min of N_2, used as internal standard, and 174 cm^3/min of He were also added. Such dilution of the feed stream was calibrated so to keep the reactants mixture in the vapour phase even at zero conversion at the reactor outlet. The activity tests were carried out at atmospheric pressure, GHSV = 2500 h^{-1} (referred to the ethanol + water gaseous mixture) at 500 °C. Additional activity tests at 400 and 300°C as well as a long term run (ca. 100 h-on stream) were also carried out on the most promising sample. Some samples were also tested at GHSV = 7755 h^{-1} to better highlight their catalytic performance.
The analysis of the out-flowing gas was carried out by a gaschromatograph (Agilent, mod. 7980) equipped with two columns connected in series (MS and Poraplot Q) with a thermal conductivity detector (TCD), properly calibrated for the detection of ethanol, acetaldehyde, acetic acid, acetone, water, ethylene, CO, CO_2, H_2. Material balance on C-containing products was checked to quantify coke deposition. Repeated analyses of the effluent gas were carried out every hour and the whole duration of every test was *ca*. 8 h. The raw data, expressed as mol/min of each species outflowing from the reactor, have been elaborated to calculate:

Products distribution [40]: Y_i = mol i / Σ(mol i)
C balance: $100 - (((\text{mol } CH_3CH_2OH * 2)_{in} - \Sigma (\text{mol } C_i * \chi_i)_{out}) / (\text{mol } CH_3CH_2OH * 2)_{in}) * 100$
Conversion: $X_i = (\text{mol i}_{in} - \text{mol i}_{out}) / \text{mol i}_{in}$ i= H_2O, CH_3CH_2OH
Selectivity: $S_i = (\text{mol i} / \nu_i) / (\text{mol ethanol}_{in} - \text{mol ethanol}_{out})$
H_2 yield: $\text{Yield} = X_{ethanol} * S_{H2} = \text{mol } H_2 / \nu_{H2} * \text{mol ethanol}_{in}$
H_2 productivity: mol H_2 out / min kg_{cat}

where *i* = products detected, dry basis; χ_i = number of C atoms in the *i*-th molecule; ν_i = stoichiometric coefficient of species *i* in the ESR reaction.

3. Results and discussion

3.1 Catalysts characterization

The catalysts were characterized by means of N_2 physisorption, in order to evaluate the effect of CaO-doping on the textural properties of the support. According to IUPAC classification [41], the non-modified sample ZNi exhibits a IV-type isotherm containing a H3-type hysteresis, typical of materials that don't possess a well-defined mesoporous structure, with a surface area of approximately 140 m^2/g (see Table 1). The isotherms of the doped samples present the same features, thus indicating that the CaO-doping neither affected the structure nor the morphology of the support.
TPR measurements (Fig. 1) were carried out, in order to identify the different NiO species on the surface of the supports and their reduction temperature.
Several reduction peaks, in a broad region between 250 and 550 °C, can be noticed in the TPR profile of ZNi. Since it is known that Ni^{2+} is reduced to Ni^0 without any intermediate oxide [42], the presence of several peaks suggests the existence of NiO species differently interacting with the support [17, 32]. The first peak can be assigned to non-interacting NiO, which is more easily reducible, since unsupported NiO reduces at about 280 °C [43, 44]. The peak at about 380 °C can

be ascribed to NiO weakly interacting with the support, while the higher temperature peaks (between 480 and 520 °C) indicates NiO species interacting stronger and stronger with zirconia [45, 46].

When analyzing the TPR profiles of the doped samples, a progressive increase of the intensity of the first peak, roughly proportional to the rise in CaO content, can be evidenced. Therefore it seems that CaO-doping increases the NiO fraction reducible at lower temperatures. In previous papers this phenomenon was correlated to a significant decrease of metal dispersion [18, 19], which negatively affected resistance to coking. Indeed, as previously reminded, smaller Ni particles are less prone to form carbon filaments. However, by looking at the crystal size variation reported in Table 1, just a small increase of Ni particle size can be observed. Therefore, according to the literature [32, 33], an increased Ni reducibility in doped samples can be ascribed to the formation of oxygen vacancies, which favor NiO reduction by weakening the Ni-O bond. These oxygen vacancies arise from the replacement of the Zr^{4+} cation with one with a lower positive charge (*i.e.* Ca^{2+}). The higher the CaO loading, the higher the concentration of oxygen vacancies and, then, of NiO species reduced at lower temperature.

XRD measurements and Rietveld refinements were carried out to determine the zirconia polymorph and ascertain if Ca^{2+} actually replaced Zr^{4+} in the lattice.

As for the support, zirconia is present only in the tetragonal phase (*i.e.* the most intense peak at $2\theta \approx 30°$), irrespective of the CaO content. Thus it may be concluded that CaO-doping did not affect the nature of the ZrO_2 polymorph of the support. Nevertheless, a regular and incremental variation of the Rietveld-refined lattice parameters as the CaO loading increased was observed (Fig. 3). The increase of the cell volume can be taken as an evidence of Zr^{4+} (ionic radii 84 pm) substitution by Ca^{2+} (ionic radii 99 pm) and supports the interpretation of the TPR results.

The crystal size of *t*-ZrO_2 also shows a regular and non-linear increase (Table 1 and Fig. 3) while the direct comparison of powder patterns and Rietveld quantitative phase analysis shows that the fraction of crystalline zirconia decreases as a function of increasing CaO content. The addition of CaO to the synthesis batch appears to hinder the nucleation of *t*-ZrO_2 thus favoring its crystal growth.

In all the samples nickel appears only in the metallic form (peak at $2\theta = 44.5°$), suggesting that the reduction treatment at 500 °C substantially reduced all Ni^{2+} to Ni^0.

Rietveld refinements of XRD patterns also provided a size estimate of Ni nanocrystals reported in Table 1. The size of Ni crystallites slightly increases with increasing CaO percentage. These data are in perfect agreement with the O_2 chemisorption results also given in Table 1.

FTIR spectroscopy of CO adsorption at RT (Room Temperature) is a well known procedure which can be resorted to, in order to evaluate the fraction of strong Lewis acidity present at the surface of oxidic materials [47]. In the present case (see Fig. 4), the admittance of 100 Torr CO onto the activated samples evidences the formation of a unique spectral envelope either in the presence or in the absence of CaO: in particular, the band that forms in all cases is located in the 2170-2180 cm^{-1}. On the basis of both spectral position and literature data [48], this band can be attributed to the ν_{CO} stretching mode of a carbonyl-like species formed between CO and coordinatively unsaturated Zr^{4+} cations located at the surface of all systems here under investigation (and set free by outgassing). However, the intensity of the band is decreasing as a consequence of the CaO loading, which might indicate that CaO is likely to bring about a sort of external coating on top of the ZrO_2 species. Moreover, the shift of the CO band (from ~2178 to ~2172 cm^{-1}) indicates that the "shielding" effect induced by the CaO species is more efficient towards the high-ν component of the CO band envelope: this, in turn, means that the highly uncoordinated Zr^{4+} cations located in the most defective crystallographic positions (like high-index side terminations of the coin-like crystallites of ZrO_2) [27] are "shielded" by the dopant. It may be then preliminary concluded that the general acidity features of the catalysts are not totally changed by the presence of CaO, rather they are partially suppressed.

The morphological features of the catalysts have been investigated by means of HR-TEM. As it can be observed, all the systems exhibit ZrO_2 particles with good crystallinity. They are highly ordered but highly packed each other as well, and with average particle size of 5-8 nm (see both images reported in Fig. 5). As far as the amount of CaO increases, a general lowering of the order is observed (see section b in Fig. 5), with the parallel evidence of an external partially amorphous habit. This amorphous overlayer is rather thin and transparent, still permitting the observation of the particles' contours.
These features are well consistent with the spectroscopic data reported in the previous section, as the decreasing intensity of the CO band is in good agreement with the partial amorphisation of the external habit of the catalysts due to the CaO dopant species. A decreased fraction of the crystalline zirconia phase, implying a larger content of the amorphous phase at high CaO loadings was also found by XRD.
It may be concluded that the specific surface area of the support did not change too much with the increased amount of CaO and therefore the Ni dispersion behaved similarly. It means that all samples are made by small and dispersed Ni nanoparticles which are essential in order to minimize coke formation.
By contrast, CaO addition to zirconia effectively reduced the Lewis acidity of the support, involved in coke deposition, and produced oxygen vacancies, which seem to affect Ni reducibility.

3.2 Activity tests

In order to check whether these modifications positively influenced the catalytic performance of the catalyst for the ESR reaction, activity tests were carried out. Table 2 shows the results of the activity tests at 500°C for every catalyst. Data reported are averaged out 4-8 h-on-stream. As already pointed out, this temperature is sufficiently high to achieve interesting catalytic performance, but it is critical as for coking and possible catalyst deactivation by this phenomenon. All the catalysts fully converted ethanol at 500°C when tested at GHSV = 2500 h^{-1}, with interesting H_2 productivity, though lower than that achieved at higher reaction temperature [18]. These conditions were chosen as practically relevant for a possible catalyst implementation. Methane was observed as the only by-product at this reaction temperature (Table 2), without acetaldehyde nor ethylene. Some selectivity towards methane formation is indeed expected at this relatively low temperature, since its formation is due to ethanol decomposition into $CH_4 + CO + H_2$, but its reforming is limited because higher reaction temperature is needed for its complete conversion. Selectivity to methane seems roughly correlated to Ni crystal size: the lowest the size, the lowest the CH_4 fraction still unreformed at 500°C, thus indicating higher activity towards SR of CH_4 for higher Ni dispersion. Furthermore, methane concentration seems roughly constant with time-on-stream and it is not correlated to possible catalyst deactivation, as is sometimes the case of ethylene and acetaldehyde.
One of the most interesting parameters to keep under control is carbon balance. Although it may be correlated to many factors, *e.g.* the formation of different species, it can be conveniently taken as index of possible catalyst coking. The C balance obtained during the blank test was 91%, with a conversion of 13%. This was attributed to some ethanol dehydration/decomposition over the quartz material filling the reactor. Additional blank test with void reactor did not evidence any ethanol conversion (< 5%) and a substantially full C balance was obtained. We already observed very limited coking activity over Ni/ZrO_2 due to very high metal dispersion (confirmed for this samples series), which limits the accumulation of carbon filaments on the active phase with its consequent possible deactivation [18]. It should be underlined that the active phase might still remain active due to simple displacement from the support also in case of extensive filaments formation. Indeed, due to accumulation of carbide species at the interface between the metal and the support, filaments growth may provoke the detachment of the metal particle from the support surface. This may not induce to complete deactivation of the particle, since Ni remains exposed to the reactants and may

still exploit it activity. However, some differences in selectivity may become evident, since for instance the support may play a role in the activation of water, providing activated oxygen or oxydril species. If the metal site is no more in contact with the support these species may not reach the CH_x species adsorbed on the metal provoking the formation of by-products. In any case, this means major modification of the sample and possible reactor failure.
The formation of carbon filaments is usually correlated with metal dispersion, *i.e*. smallest Ni particles are expected to form less filaments. We indeed observed such a correlation in other sets of catalysts in which a significant variation of Ni crystal size was present. In the present case, a substantially similar Ni dispersion should result in similar coking activity, or at least we would expect a trend of C balance opposite to Ni crystal size. By contrast, C balance was found also correlated to CaO loading.
Some coking might also occur due to ethylene polimerisation over acidic sites of the support. Therefore, acidity tuning achieved by this samples set may help limiting this additional coking feature.
Carbon balance slightly increased upon doping with CaO, reaching its maximum at the highest loading. In particular, it can be noted (Fig. 6) that carbon balance decreased significantly within 8 h-on-stream for sample ZNi, whereas it was stable and almost complete for ZCa_9Ni.
Since H_2 productivity and ethanol conversion did not change significantly, we may conclude that acidity limitations brought about by the addition of CaO may be beneficial in depressing coking activity due to surface acidity.
Additional tests have been carried out at higher space velocity (7755 h^{-1}) for samples ZNi and ZCa_9Ni in order to better highlight their differences at lower conversion (Table 3). The catalytic activity on sample ZNi was in general worse than that of the Ca-doped one. Indeed, the steady state conversion was lower and the sample was mainly selective to acetaldehyde. By contrast, the activity of sample ZCa_9Ni was stable with time-on-stream and allowed to reach significant H_2 productivity in spite of the presence of unreformed by-products, whose selectivity remained as well constant for the whole duration of the test.
The presence of unreformed ethylene is also interesting for ZCa_9Ni. Indeed, its concentration remained stable for the whole duration of the test, indicating its incomplete reforming under these conditions, but contemporarily negligible coke formation by its polimerisation over the catalyst surface. By contrast, some unreformed ethylene (15% selectivity) was evidenced during the first 2 h-on-stream for ZNi, accompanied by higher ethanol conversion. Then ethylene disappeared from the reaction products, likely accumulating over the acidic sites of the support, and this was accompanied by a decrease of ethanol conversion, then stabilized to 35%. The difference of carbon balance was lower in this case. Indeed, the main contribution of C accumulation by filaments formation over Ni particles is limited by the very low ethanol decomposition activity. Indeed, if less carbide precursor species are present over the metal their accumulation in the form of nanotubes is unlikely.
Focusing our attention on sample ZCa_9Ni, particularly promising as for resistance to coking, we additionally performed activity tests at lower temperature at GHSV = 2500 h^{-1} (Table 4).
Ethanol conversion unacceptably decreased when cooling the reactor down to 400°C and it was even lower at 300°C (*ca.* 0.05). Furthermore, at 400°C the major byproduct was ethylene, with selectivity increasing with time-on-stream, though acetaldehyde also formed. The carbon balance at such temperature became unacceptably low and decreasing with time-on-stream. This may suggest that carbon accumulation occurred at 400°C over the catalyst surface, likely in the form of polymers partially and progressively covering the active phase, which indeed decreased its activity with time-on-stream. Thus 500°C was considered the lowest temperature to achieve satisfactory activity testing for this application.
At the end of activity tests at lower temperature, the reactor was heated up again at 500°C and a prolonged run was carried out for 5 days on the same ZCa_9Ni sample. At first one may notice that test d1 in Table 3 recovered roughly the same results of the test on the freshly activated sample,

ruling out the hypothesis of irreversible deactivation due to severe coking of the active phase at 400 and 300°C. Likely, coke gasification occurred when increasing temperature at 500°C allowing to recover the full activity of the active phase. Catalyst performance remained stable for *ca*. 100 h-on-stream, without any decrease of ethanol conversion. Some acetaldehyde started forming after ca. 50 h-on-stream, whereas ethylene was never observed at reactor outlet.
The addition of a basic promoter showed beneficial in improving catalyst resistance towards coking. These results can be ascribed to the progressive decrease of the Lewis acidity of the support, which contributes to the side reactions leading to coke deposition. In average, a higher C balance, *i.e.* lower coking, was achieved with sample ZCa_9Ni.
CaO doping also induces the formation of oxygen vacancies, proportionally to its concentration. Oxygen vacancies may activate CO_2 and H_2O, thus favouring the gasification of coke [32, 49, 50]. This, coupled with the very small Ni particle size and to titration of the strongest acid sites helps in keeping under control coke deposition under critical reaction conditions.
In order to better characterise the coking phenomenon, the spent catalysts were characterised by means of Micro-Raman, TEM and FE-SEM.
Micro-Raman analysis (Fig. 7) evidenced the presence of both the D and G bands of graphite that were attributed to the presence of multiwalled carbon nanotubes (MWCNTs) and to encapsulating coke due to polymerization [51, 52]. Some C was observed over the surface of sample ZCa_9Ni, e.g. graphite layers visible in Fig. 8. This has been likely loaded on the catalyst during low temperature testing and it is likely localised over the support surface, leaving substantially unaltered the active phase. On the contrary, catalyst ZNi was predominantly characterised by the contribution of ordered carbon. The latter was constituted by MWCNTs, 33-37 nm in diameter, as depicted in Fig. 8 and 9, which were completely absent in sample ZCa_9Ni.
The spent catalysts have been characterized also by TPO analysis. The sample ZNi used for the standard activity testing (8 h-on-stream at 500°C) returned a carbon deposition rate of 10.1 mg C/g_{cat} h. Sample ZCa_9Ni, tested after the durability test (5 days-on-stream) evidenced a much more limited C accumulation, corresponding to a rate of 0.75 mg C/g_{cat} h. These data were also semiquantitatively confirmed by EDX analysis.
Therefore, we can conclude that some accumulation of coke may be due to ethanol dehydration to ethylene, which may polymerise at relatively low temperature if it is not efficiently gasified. The titration of the strongest acidic sites with CaO may limit this phenomenon and additionally it can provide oxygen vacancies acting as activation sites for water and carbon dioxide, which helps cleaning the surface of the active phase.
MWCNTs may also form, promoted by Ni itself, especially when poorly dispersed or not sufficiently stabilised by the support. Therefore, in spite of the high Ni dispersion, similar for samples ZNi and ZCa_9Ni, CNTs were evident in the spent ZNi sample. Hence, we may additionally conclude that doping with CaO, and the consequent oxygen vacancies formation, helps in cleaning up the surface by providing activated OH or O radicals, which are also able to stop the subsurface accumulation of carbon at the interface between Ni and the support. This effectively inhibits the growth of CNTs.

4. Conclusions

Ni/ZrO_2 proved to be highly active in ethanol steam reforming. Nevertheless, the presence of Lewis acid sites on the surface of the support, due to coordinatively unsaturated Zr^{4+} ions, was probably related to the coke formation which slightly deactivated the catalyst. The addition of CaO to the support was effective in reducing the Lewis acidity of zirconia and improving catalyst resistance towards coking. Moreover, CaO addition was responsible for the formation of oxygen vacancies, that can activate CO_2 and H_2O, thus favouring the gasification of coke. The latter also inhibited the growth of multiwalled carbon nanotubes. On the contrary, CaO-doping did not affect Ni dispersion,

so Ni nanoparticles were small and dispersed in all samples, which is essential in order to minimize coke formation.

Acknowledgements

The authors are indebted to Agnieszka Iwanska for the excellent technical assistance. The valuable help of Giacomo Mariani,Alessio Sozzi and Matteo Compagnoni in collecting activity data and for the characterization of spent catalysts is gratefully acknowledged. The work was partly supported by H2FC European Infrastructure Project (Integrating European Infrastructure to support science and development of Hydrogen and Fuel Cell Technologies towards European Strategy for Sustainable Competitive and Secure Energy), project reference 284522.

References

[1] B. Zhang, X. Tang, Y. Li, Y. Xu, W. Shen, Int. J. Hydrogen Energy. 32 (2007) 2367-2373.
[2] A. Carrero, J.A. Calles, A.J. Vizcaíno, Appl. Catal. A: General. 327 (2007) 82-94.
[3] A. Birot, F. Epron, C. Descorme, D. Duprez, Appl. Catal. B: Environ. 79 (2008) 17-25.
[4] M. Benito, J.L. Sanz, R. Isabel, R. Padilla, R. Arjona, L. Daza, J. Power Sources. 151 (2005) 11-17.
[5] A. Haryanto, S. Fernando, N. Murali, S. Adhikari, Energy Fuels. 19 (2005) 2098-2106.
[6] D.L. Trimm, Catal. Today. 37 (1997) 233-238.
[7] A.N. Fatsikostas, X.E. Verykios, J. Catal. 225 (2004) 439-452.
[8] R.R. Davda, J.W. Shabaker, G.W. Huber, R.D. Cortright, J.A. Dumesic, Appl. Catal. B: Environ. 43 (2003) 13–26.
[9] R.R. Davda, J.W. Shabaker, G.W. Huber, R.D. Cortright, J.A. Dumesic, Appl. Catal. B: Environ. 56 (2005) 171–186.
[10] Z. Zhang, X.E. Verykios, Appl. Catal. A: General. 138 (1996) 109-133.
[11] G. Centi, S. Perathoner, Catal. Today 148 (2009) 191-205.
[12] V.M. Gonzalez-DelaCruz, J.P. Holgado, R. Pereníguez, A. Caballero, J. Catal. 257 (2008) 307-314.
[13] K.O. Christensen, D. Chen, R. Lødeng, A. Holmen, Appl. Catal. A: General 314 (2006) 9-22.
[14] D. Chen, K.O. Christensen, E. Ochoa-Fernandez, Z. Yu, B. Tøtdal, N. Latorre, A.Monzòn, A. Holmen, J. Catal. 229 (2005) 82-96.
[15] A. Iriondo, V.L. Barrio, J.F. Cambra, P.L. Arias, M.B. Guemez, M.C. Sanchez-Sanchez, R.M. Navarro, J.L.G. Fierro, Int. J. Hydrogen Energy. 35 (2010) 11622-11633.
[16] M. Lindo, A.J. Vizcaíno, J.A. Calles, A. Carrero, Int. J. Hydrogen Energy. 35 (2010) 5895-5901.
[17] V. Nichele, M. Signoretto, F. Menegazzo, A. Gallo, V. Dal Santo, G. Cruciani, G. Cerrato, Appl. Catal. B: Environ. 111-112 (2012) 225-232.
[18] I. Rossetti, C. Biffi, C.L. Bianchi, V. Nichele, M.Signoretto, F. Menegazzo, E. Finocchio, G. Ramis, A. Di Michele, Appl. Catal. B: Environ. 117-118 (2012) 384-396.
[19] I. Rossetti, A. Gallo, V. Dal Santo, C.L. Bianchi, V. Nichele, M. Signoretto, E. Finocchio, G. Ramis, A. Di Michele, ChemCatChem. 5 (2013) 294-306.
[20] A. Le Valant, F. Can, N. Bion, D. Duprez, F. Epron, Int. J. Hydrogen Energy. 35 (2010) 5015-5020.
[21] A.J. Vizcaíno, A. Carrero, J.A. Calles, Int. J. Hydrogen Energy.32 (2007) 1450-1461.
[22] S. Cavallaro, N. Mondello, S. Freni, J. Power Sources. 102 (2001) 198-204.
[23] M.H. Youn, J.G. Seo, H. Lee, Y. Bang, J.S. Chung, I.K. Song, Appl. Catal. B: Environ. 98 (2010) 57-64.
[24] G. Wen, Y. Xu, H. Ma, Z. Xu, Z. Tian, Int. J. Hydrogen Energy. 33 (2008) 6657-6666.
[25] K.G. Azzam, I.V. Babich, K. Seshan, L. Lefferts, J. Catal. 251 (2007) 153-162.
[26] C Morterra, G Cerrato, M. Signoretto, Catal. Lett. 41 (1996) 101-109.
[27] C. Morterra, G. Cerrato, V. Bolis, S. Di Ciero, M. Signoretto, J. Chem. Soc., Faraday Trans. 93(6) (1997) 1179-1184.
[28] C. Morterra, G. Cerrato, S. Di Ciero, Appl. Surf. Sci. 126 (1998) 107-128.
[29] J.A. Calles, A. Carrero, A.J. Vizcaíno, Micropor. Mesopor. Mater. 119 (2009) 200.207.
[30] Z. Hou, O. Yokota, T. Tanaka, T. Yashima, Appl. Catal. A: General. 253 (2003) 381-387.
[31] J. da S. Lisboa, D.C.R.M. Santos, F.B. Passos, F.B. Noronha, Catal. Today. 101 (2005) 15-21.
[32] J.D.A. Bellido, E.M. Assaf, J. Power Sources. 177 (2008) 24-32.
[33] J.D.A. Bellido, J.E. De Souza, J.C. M'Peko, E.M. Assaf, Appl. Catal. A: General. 358 (2009) 215-223.
[34] S. Liu, L. Guan, J. Li, N. Zhao, W. Wei, Y. Sun, Fuel. 87 (2008) 2477-2481.
[35] M.S. Fan, A.Z. Abdullah, S. Bhatia, Appl. Catal. B: Environ. 100 (2010) 365-377.

[36] F. Zane, S. Melada , M. Signoretto, F. Pinna, Appl. Catal. A: General. 299 (2006) 137-144.
[37] S. Brunauer, P.H. Emmett, E. Teller, J. Am. Chem. Soc. 60 (1938) 309-319.
[38] E.P. Barrett, L.G. Joyner, P.P. Halenda, J. Am. Chem. Soc. 73 (1951) 373-380.
[39] J.S. Smith, P.A. Thrower, M.A. Vannice, J. Catal. 68 (1981) 270-285.
[40] M. Benito, R. Padilla, A. Serrano-Lotina, L. Rodríguez, J.J. Brey, L. Daza, J. Power Sources. 192 (2009) 158-164.
[41] IUPAC Recommendations, Pure Appl. Chem. 57 (1985) 603-619.
[42] Y.J.O. Asencios, E.M. Assaf, Fuel Process. Technol. 106 (2013) 247-252.
[43] L. Zhang, J. Lin, Y. Chen, J. Chem. Soc. Faraday Trans. 88 (14) (1992) 2075-2078.
[44] Q.G. Yan, W.Z. Weng, H.L. Wan, H. Toghiani, R.K. Toghiani, C.U. Pittman, Jr, Appl. Catal. A: General. 239 (2003) 43-58.
[45] Y.Q. Song, D.H. He, B.Q. Xu, Appl.Catal. A: General. 337 (2008) 19-28.
[46] V. García, J.J. Fernández, W. Ruíz, F. Mondragón, A. Moreno, Catal. Commun. 11 (2009) 240-246.
[47] G. Herzberg, Molecular Spectra and Molecular Structure. II. Infrared and Raman Spectra of Polyatomic Molecules, Van Nostrand Co., New York, 1947, p. 274.
[48] G. Cerrato, S. Bordiga, S. Barbera, C. Morterra, Surf. Sci. 50 (1997) 377-379.
[49] Y.J.O. Asencios, J.D.A. Bellido, E.M. Assaf, Appl. Catal. A: General. 397 (2011) 138-144.
[50] T. Horiuchi, K. Sakuma, T. Fukui, Y. Kubo, T. Osaki, T. Mori, Appl. Catal. A: General. 144 (1996) 111-120.
[51] C. Gao, Y. Z. Jin, H. Kong, R.L.D. Whitby, S.F. A. Acquah, G.Y. Chen, H. Qian, A. Hartschuh, S.R.P. Silva, S. Henley, P. Fearon, H.W. Kroto, D.R.M. Walton, J. Phys. Chem. B, 109 (2005) 11925.
[52] P. Delhaes, M. Couzi, M. Trinquecoste, J. Dentzer, H. Hamidou, C. Vix-Guterl, Carbon, 44 (2006) 3005.

Table captions

Tab. 1: Specific surface area and crystal size (*c.s.*) of catalysts as determined by O_2 chemisorption and Rietveld refinement.
Tab. 2: Results of the activity tests for ethanol steam reforming at 500 °C. Time-on-stream: 8 hours, data averaged out 4-8 h-on-stream, GHSV = 2500h^{-1}.
Tab. 3: Results of the activity tests for ethanol steam reforming at 500 °C. Time-on-stream: 8 hours, data averaged out 4-8 h-on-stream, GHSV = 7755 h^{-1}.
Table 4: Results of the activity tests for ESR of sample ZCa_9Ni at different temperature and durability test at 500°C for 5 days. T-o-s: time-on-stream; d1-d5: days 1 to 5; GHSV = 2500 h^{-1}.

Tables

Tab. 1

	ZNi	**ZCa$_3$Ni**	**ZCa$_6$Ni**	**ZCa$_9$Ni**
Specific surface area / m^2 g^{-1}	141	150	142	135
***c.s.*$_{ZrO2}$ Rietveld / nm**	7.3	8.1	9.3	13.4
***c.s.*$_{Ni}$ Rietveld / nm**	3.2	2.8	3.4	4.5
d$_{Ni}$ O$_2$ chemisorption / nm	4.5	3.8	4.6	5.4

Tab. 2

	Blank test	**ZNi**	**ZCa_3Ni**	**ZCa_6Ni**	**ZCa_9Ni**
EtOH conversion / %	13 ± 5	100 ± 0	100 ± 0	100 ± 0	100 ± 0
C balance / %	91 ± 2	88 ± 4	89 ± 4	89 ± 3	95 ± 3
H_2 productivity / mol/min kg_{cat}	-	0.96 ± 0.05	0.9 ± 0.1	0.96 ± 0.08	0.86 ± 0.05
CH_4 selectivity / %	-	17.3 ± 0.4	3.4 ± 1.0	7.2 ± 1.2	13 ± 1

Tab. 3

	ZNi	ZCa_9Ni
EtOH conversion / %	35 ± 7	53 ± 8
C balance / %	93 ± 6	100 ± 4
H_2 productivity / mol/min kg_{cat}	n.d.	1.94 ± 0.10
Sel. CH_4 (%)	0	6.4 ± 1.0
Sel. CH_3CHO (%)	55 ± 11	35 ± 5
Sel. CH_2CH_2 (%)	0	4.9 ± 0.7

Tab. 4

	500°C	400°C	500°C_d1	500°C_d2	500°C_d3	500°C_d4	500°C_d5
EtOH conversion / %	100 ± 0	62 ± 9 (decreasing with t-o-s)	100 ± 0	100 ± 0	100 ± 0	100 ± 0	100 ± 0
C balance / %	95 ± 3	74 ± 11	91 ± 4	92 ± 6	91 ± 7	94 ± 2	89 ± 4
H_2 productivity / mol/min kg_{cat}	0.86 ± 0.05	0.3 ± 0.4	0.84 ± 0.05	0.85 ± 0.03	0.82 ± 0.06	0.84 ± 0.05	0.80 ± 0.03
Sel. CH_4 (%)	13 ± 1	2.1 ± 0.5	12 ± 2	14 ± 2	13 ± 4	13 ± 1	12 ± 2
Sel. CH_3CHO (%)	0	7 ± 2	0	0	1.1 ± 1.0	2.5 ± 0.4	1.7 ± 1.0
Sel. CH_2CH_2 (%)	0	20 ± 5 (increasing with t-o-s)	0	0	0	0	0

Figure captions

Fig. 1: TPR profiles of the catalysts with various CaO loadings.
Fig. 2: XRD powder patterns of the reduced catalysts at increasing Ca content (from bottom to top).
Fig. 3: Relative variation of the lattice parameters (ratios of unit-cell constants, a/a_0 and c/c_0, and volume, V/V_0, where a_0, c_0, and V_0 are the parameters of *t*-ZrO_2 without Ca) and crystal size of the zirconia phase as a function of the CaO loading.
Fig. 4: FTIR spectra of adsorbed CO at RT on the reduced catalysts.
Fig. 5: TEM images of: a) ZNi; b) ZCa_9Ni.
Fig. 6: Trend of C balance with time-on-stream for: a) ZNi; b) ZCa_9Ni.
Fig. 7: Microraman spectra of the spent sample ZNi.
Fig. 8: TEM micrographs of spent samples ZNi (a, b) and ZCa_9Ni (c, d).
Fig. 9: FE-SEM images of spent samples ZNi (a, b) and ZCa_9Ni (c, d).

Figures

Fig. 1

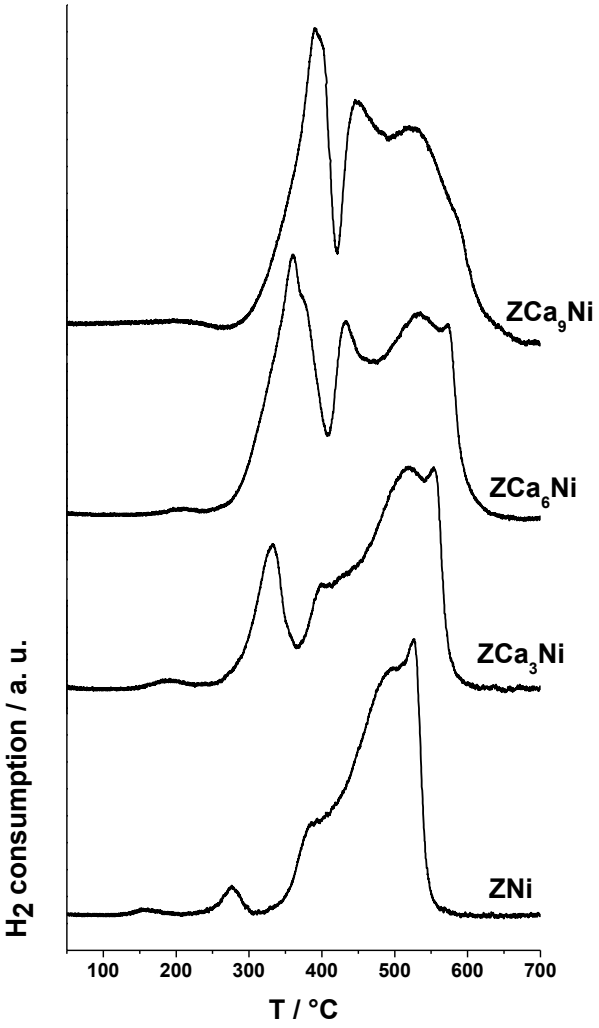

Fig. 2

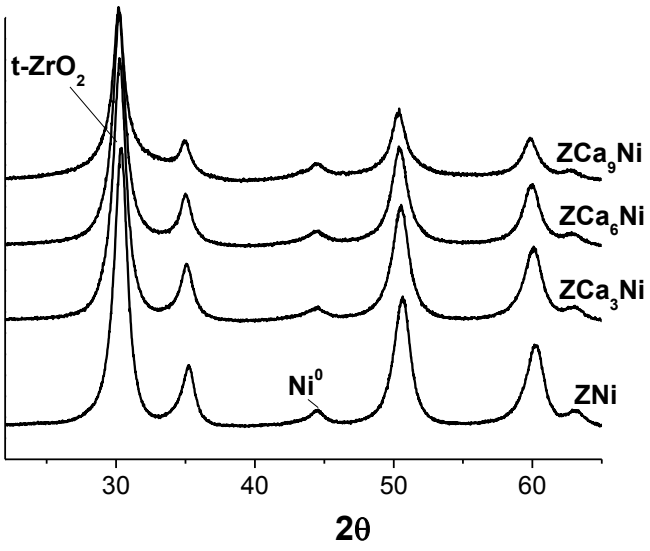

Fig. 3

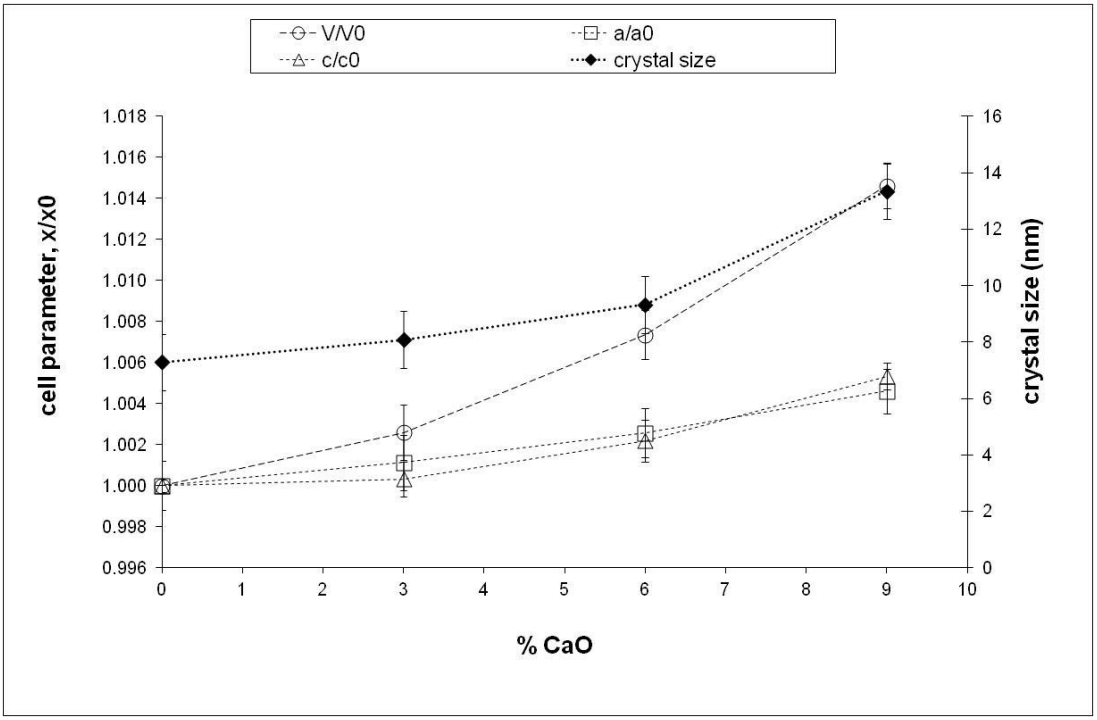
V/V0
a/a0
c/c0
crystal size
cell parameter, x/x0
crystal size (nm)
% CaO
1.018
1.016
1.014
1.012
1.010
1.008
1.006
1.004
1.002
1.000
0.998
0.996
16
14
12
10
8
6
4
2
0
0
1
2
3
4
5
6
7
8
9
10

Fig. 4

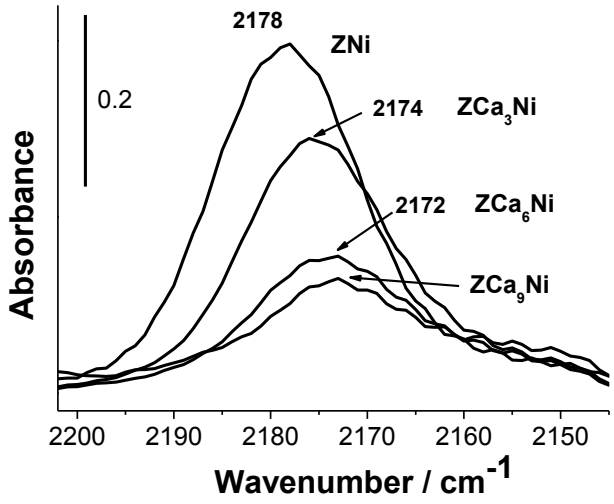
2178
ZNi
0.2
2174
ZCa3Ni
2172
ZCa6Ni
ZCa9Ni
Absorbance
2200
2190
2180
2170
2160
2150
Wavenumber / cm-1

Fig. 5

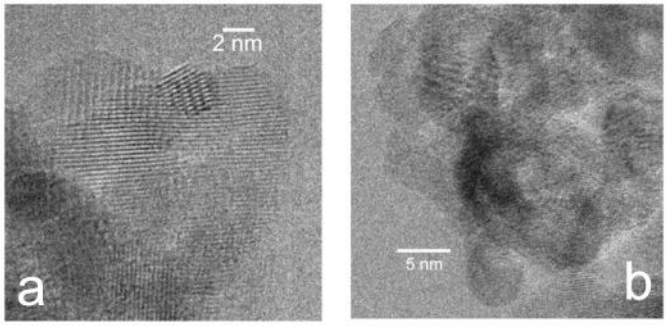

Fig. 6

a)

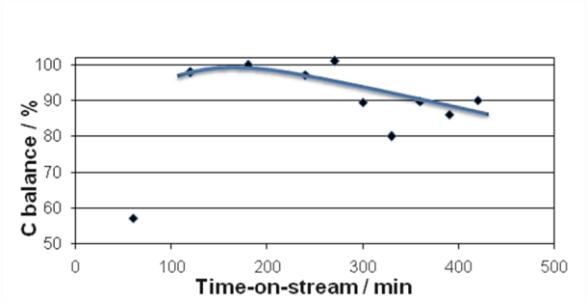
C balance / %
100
90
80
70
60
50
0
100
200
300
400
500
Time-on-stream / min

b)

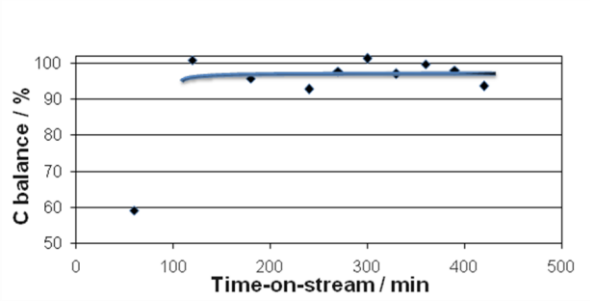
C balance / %
100
90
80
70
60
50
0
100
200
300
400
500
Time-on-stream / min

Fig. 7

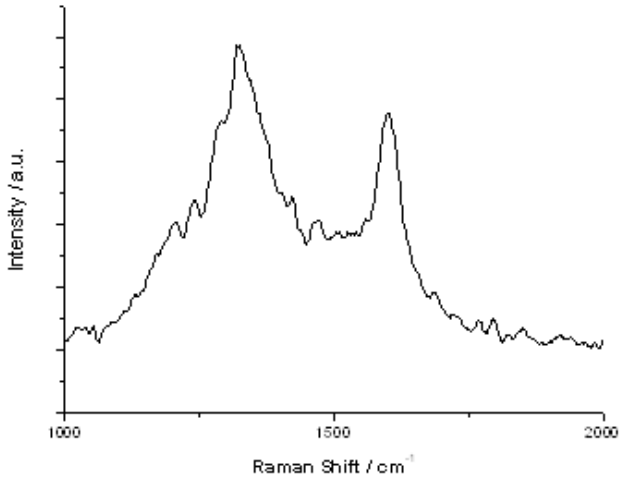

Fig. 8

a) 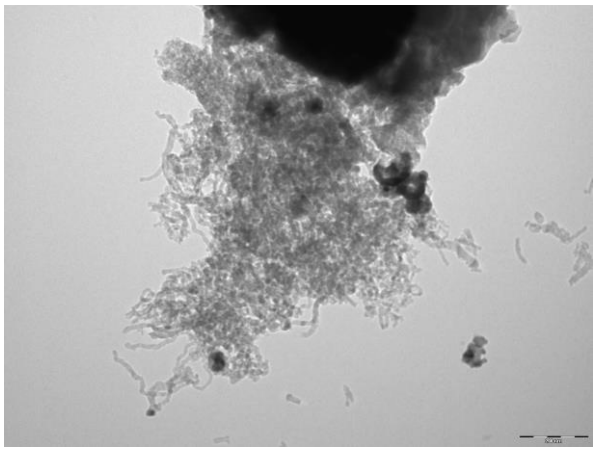

b) 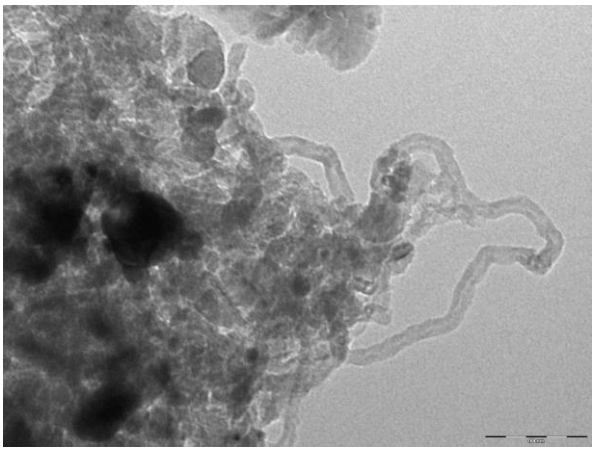

c) 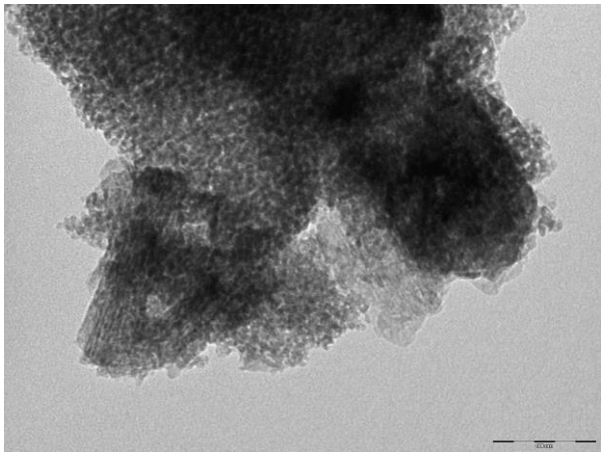

d) 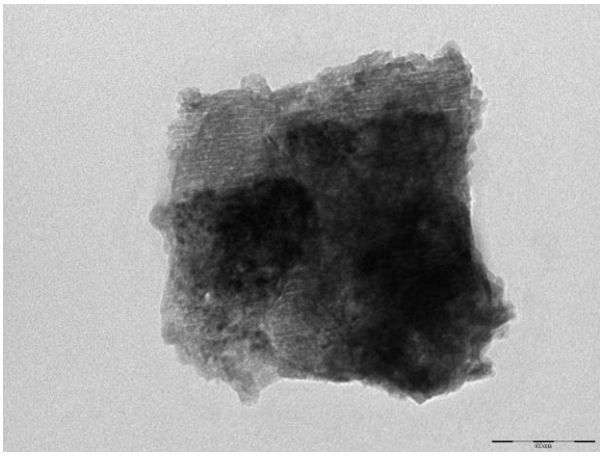

Fig. 9

a) 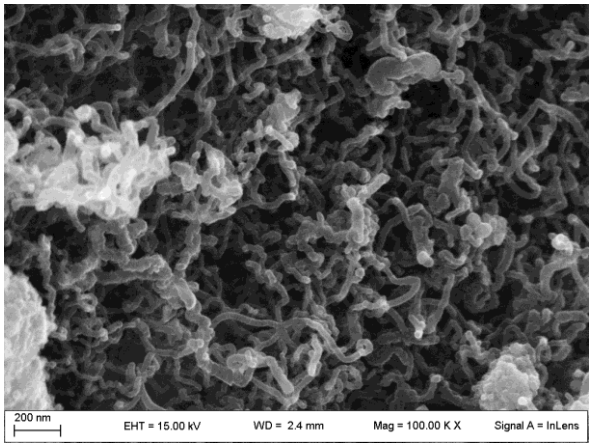
200 nm
EHT = 15.00 kV
WD = 2.4 mm
Mag = 100.00 K X
Signal A = InLens

b) 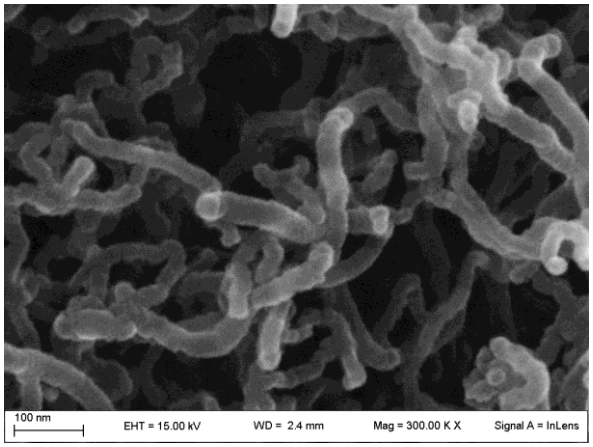
100 nm
EHT = 15.00 kV
WD = 2.4 mm
Mag = 300.00 K X
Signal A = InLens

c) 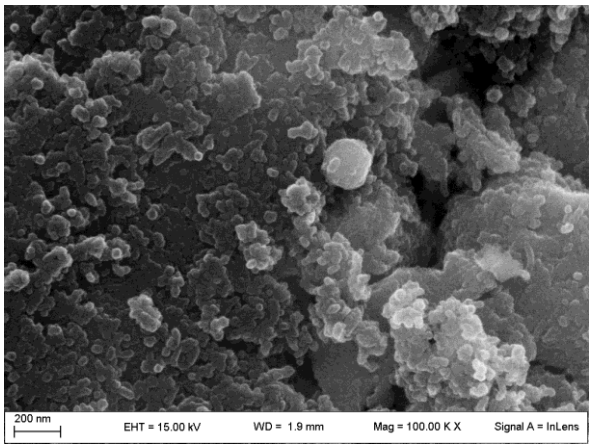
200 nm
EHT = 15.00 kV
WD = 1.9 mm
Mag = 100.00 K X
Signal A = InLens

d) 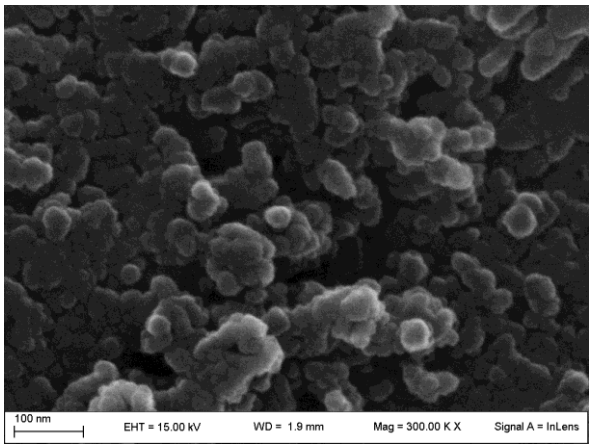
100 nm
EHT = 15.00 kV
WD = 1.9 mm
Mag = 300.00 K X
Signal A = InLens